actuators

MDPI

Article

A Multidirectional Forearm Electromagnetic Generator Designed via Numerical Simulations

Nanfei He [1], Colton King [2], Qizheng Xie [2], Feng Zhao [3] and Wei Gao [1,*]

[1] Department of Textile Engineering, Chemistry and Science, North Carolina State University, Raleigh, NC 27606, USA; nhe@ncsu.edu
[2] North Carolina School of Science and Mathematics, Durham, NC 27705, USA
[3] Storagenergy Technologies, Inc., Salt Lake City, UT 84104, USA
* Correspondence: wgao5@ncsu.edu

Abstract: Harvesting biomechanical energy from daily human body motions provides a promising and sustainable power solution for wearable electronics, whose current power supplies, i.e., batteries, have unsatisfactory capacity and durability due to volume, shape, and flexibility constraints. Electromagnetic generators (EMGs) are favorable energy transducers because of their high energy-conversion efficiency, low dependence on frequencies, and long-term stability. However, an EMG that can effectively harvest energy from multi-directional arm motions at aperiodic low frequencies are yet to be created. Here, we introduce a unique EMG configuration by combining a linear and a helix frame into a monolithic unit (EMG-LH), enabling the EMG to scavenge energy from all kinds of arm motions up to 6 degrees of freedom (DOFs) (movement along XYZ axes and forearm rotations). The EMG frame geometry is designed and optimized according to numerical simulations. To clarify the working mechanism and maximize the power output, the copper coils' winding pattern, the magnets' velocity profiles, and the resulting voltage output are numerically simulated and then experimentally verified. Our EMG-LH outperforms linear EMGs (EMG-Ls) and helix EMGs (EMG-Hs) in harvesting energy from all arm motions. This work explicitly presents a forearm-wearable energy harvester as a sustainable power source for wearable electronics.

Keywords: electromagnetic; energy harvesting; wearable; body movement; multi-directional; numerical simulation

Citation: He, N.; King, C.; Xie, Q.; Zhao, F.; Gao, W. A Multidirectional Forearm Electromagnetic Generator Designed via Numerical Simulations. *Actuators* **2023**, *12*, 225. https://doi.org/10.3390/act12060225

Academic Editor: Yi-Chung Shu

Received: 26 April 2023
Revised: 24 May 2023
Accepted: 26 May 2023
Published: 29 May 2023

1. Introduction

The advancing of wearable and portable electronics poses great challenges on their energy supply units [1,2]. Miniaturized rechargeable batteries remain the major solutions now, but they are limited in storage capacity due to the size and flexibility constraints, leading to unsatisfactory battery life [1,3]. Harvesting biomechanical energy from daily human motions can be a sustainable solution for this [4,5]. Different approaches based on electromagnetic [6,7], piezoelectric [8,9], and triboelectric mechanisms [10,11] have been extensively explored, while we consider electromagnetic generators (EMGs) among the best options in wearable scenarios [12], primarily due to their high energy-conversion efficiency and long-term stability as compared to triboelectrics, and higher power output and lower frequency dependence as compared to piezoelectrics [3,13,14].

Linear magnet–spring EMGs have been traditionally adopted to harvest energy from one-dimensional oscillations [15,16]. Generally, linear EMGs achieve optimal performance when external exciting frequency matches their resonant frequencies, and they experience great power loss once the exciting frequency drifts away [15]. Additionally, they tend to perform poorly under nonperiodic low-frequency vibrations, which unfortunately are dominating among daily motions of the human body [17]. Targeting at harvesting energy from random human motions, numerous studies have focused on enlarging the

response frequency range of linear EMGs, for example, by using nonlinear spring [18], bi-stable spring [19], or magnetic spring [20]. In addition, different frequency-up conversion strategies [21,22] are introduced to convert low-frequency vibrations into high-frequency motions. By introducing certain distances to allow a magnet to move freely inside an EMG frame, Haroun et al. [23] presented EMGs with a broad frequency bandwidth that can effectively harvest energy at low frequencies.

Besides the nonperiodic low-frequency feature, arm motions vary in directions up to 6 degrees of freedoms (DOFs) [24], which require EMGs to scavenge energy along more than one direction. Though linear EMGs are being optimized to harvest energy from low-frequency vibrations, they are limited to a specific direction of arm motion, largely restraining their energy harvesting efficiency. To improve energy conversion efficiency, EMGs in different geometries have emerged to allow magnet–coil relative motions upon various arm shifts. Abdul Samad et al. designed a curved EMG fixed along the forearm to harvest energy from two directions of arm movements [25]. Circular wrist wearable EMGs have been developed to harvest energy from arm swing and wrist rotation [26–28]. Compared to linear EMGs, circular-shaped EMGs can function in different motion scenarios, but they are yet to adapt to all six DOFs, making them far from efficient in energy harvesting from daily forearm motions.

Magnet–coil configurations also play a critical role in maximizing the power output of EMGs. Researchers investigated the use of alternating polarity magnet arrays to induce abrupt magnetic flux density change for increased power output [29,30]. Spreemann et al. simulated the magnetic field distribution of solenoid coils to identify the optimal position of a magnet within the coil, which leads to the maximum flux gradient and, thereby, the maximum voltage output. This is considered as the equilibrium point of their microscale vibration EMGs that feature a resonant mass/spring system [16]. Wang et al. [31] concluded from numerical analysis that, when the central plane of the coil is at the midpoint of the linear EMG frame, their piecewise device offers the highest voltage output. Based on simulation results, Haroun et al. [23,32] discussed the relationship between magnetic flux gradient and magnet relative position within a coil. Though the magnet–coil relationship has been studied in different EMG geometries via simulations, they are rarely experimentally verified and the effect of specific coil parameters, such as the coil widths, coil winding directions, etc., on the instantaneous voltage response as magnet passes through coils has not yet been investigated in detail in wearable scenarios.

In this work, targeting an EMG which can effectively harvest energy from different forearm motions in daily activities, we introduce a unique EMG configuration by combining a linear and a helix frame into a monolithic piece (EMG-LH) in order to take advantage of both geometries in a wearable setting. This peculiar design allows magnets to move freely within the frame tube upon random, multi-dimensional arm motions at low frequencies, thus achieving high energy-harvesting efficiency. The EMG frames in optimal geometries are designed according to our mathematical simulations and later embodied via 3D printing. To analyze the working principle and maximize the power output of EMGs, the copper coil winding patterns, the magnet motions, and the resulting voltage output are both numerically simulated and experimentally verified. A decent match between the two has been observed in our experiments. The EMG-LHs outperform linear EMGs (EMG-Ls) and helix EMGs (EMG-Hs), superior in harvesting energy from 6 DOF forearm motions, with a reasonable mass of 42.79 $\pm$ 0.97 g to ensure wearability. This work explicitly presents a forearm-wearable energy harvester which can function as a sustainable power source for wearable electronics.

2. Results and Discussion

The proposed electromagnetic energy harvester is based on the relative oscillation between a permanent magnet and a set of copper coils. A forearm-wearable frame is designed into a proper shape to house the magnet and mount coils. The inertia of the magnet mass causes it to move relative to the coil-wound frame when the frame experiences

acceleration upon arm motions. According to Faraday's law, the induced electromotive force (*emf*) is given by:

$$emf = -\frac{d\varphi}{dt} = -\frac{d\varphi}{dz}\frac{dz}{dt} = k_t\dot{z} \quad (1)$$

where k_t is the transduction factor (i.e., $\frac{d\varphi}{dz}$, magnetic flux gradient), which depends on the strength of the magnet and coil configurations, and $\dot{z}$ is the relative velocity between the magnet and the coil.

The output electrical power is expressed as:

$$P = \frac{emf^2}{R} = \frac{(k_t\dot{z})^2}{R} \quad (2)$$

where R is the total resistance of the circuit. Only the coil resistance (R_{coil}) is considered in calculating the maximum output power.

As revealed by Equations (1) and (2), to maximize the power generated by EMGs, the frame geometries that dictate magnet movement pathways should be designed to allow the magnet to reach the highest possible $\dot{z}$. Meanwhile, coil configurations with optimum k_t should be constructed to convert as much mechanical energy into electrical energy as possible. Additional considerations include wrist wearability and energy-harvesting effectiveness from multi-dimensional arm motions at aperiodic low frequencies. Figure 1a–e shows the proposed EMG-LH design that can harvest energy from arm motions in multi-DOFs (movement along XYZ axes (Figure 1a–d) and forearm rotation (Figure 1e)). Combining the linear and helix parts allows the magnet to travel among different coil segments upon all kinds of arm motions (Figure 1f).

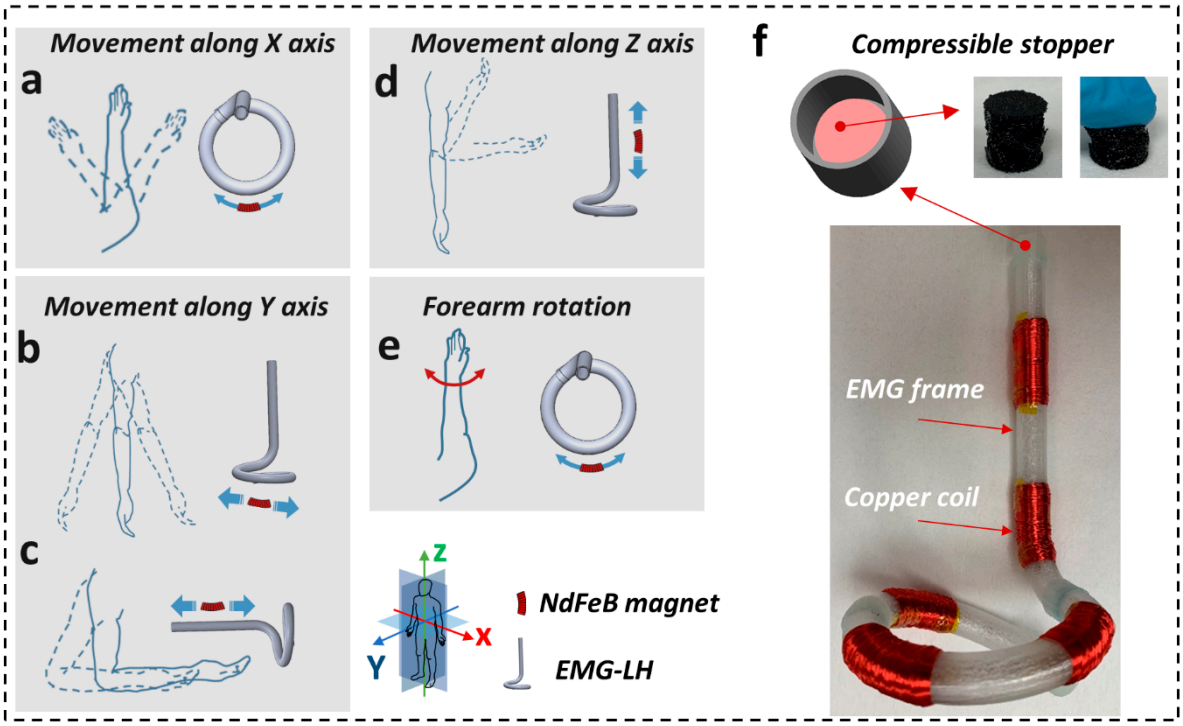

Figure 1. (**a**–**e**) Schematics of magnet movements within EMG-LH under different forearm motions: (**a**) forearm movement along *x* axis; (**b**) forearm movement along *y* axis with straight elbow; (**c**) forearm movement along *y* axis with bent elbow; (**d**) forearm movement along *z* axis; (**e**) forearm rotation; (**f**) photographs of as-fabricated EMG-LH and a schematic of the compressible end stopper.

2.1. Coil Configuration Optimization

The induction coil is an essential part of any electromagnetic energy harvester. It is of great importance to understand the effect of coil configurations on the profile of transduction factor k_t as the magnet moving through it. Coil configurations can be defined by coil width (W) and the direction of coil winding. Orthocyclic winding in which turns are arranged side by side is adopted to create densely packed coils [33]. Ten thin disk-shaped magnets (8 mm × 1.6 mm) are stacked together to form a magnet assembly (8 mm × 16 mm). The parameters of the copper wires, the magnets, and the frames used in our EMGs are presented in Table S1. The relationship between the magnetic flux gradient ($d\varphi/dz$), i.e., k_t, and the position of the magnet relative to the coil (z) can be simulated according to Equation (3) [23,34]:

$$\frac{d\varphi}{dz} = N_l \frac{\mu_0 m}{2} \sum_{n=-N_t/2}^{n=N_t/2} z_n \left[\frac{3{z_n}^3}{\left(r^2 + {z_n}^2\right)^{5/2}} - \frac{3}{\left(r^2 + {z_n}^2\right)^{3/2}} \right] \quad (3)$$

$$z_n = z + n\left(\frac{W}{N_t - 1}\right)$$

where N_l is the number of coil layers; N_t is the number of coil turns within each layer; m is the magnetic moment; μ_0 is the permeability of the free space; and r is the coil mean radius.

In terms of winding directions of the turns in a coil, other than winding all turns in the same direction (Figure 2a inset schematic), a coil can be a combination of two serially connected and oppositely wound coil segments, with one in a clockwise direction towards the right (R) and the other in counterclockwise towards the left (L) direction (coil-RL) (Figure 2b inset schematic). To distinguish from coil-RL, the coil with all turns in one direction is named as coil-RR. Figure 2a demonstrates the simulated behavior of $d\varphi/dz$ for coil-RR under different coil widths with respect to the position of the magnet relative to the coil (z). The simulation results indicate no energy conversion when the magnet moves across the middle region of the coils, since the magnetic field gradient ($d\varphi/dz$) is close to zero. As W increases from 10 mm to 50 mm, this central ineffective region also expands. Two oppositely directed peaks of $d\varphi/dz$ occur at the edges of the coil, while the peak widths and heights do not significantly change as coil widths vary, especially after W exceeding 20 mm, suggesting that extra turns in coil-RR ($W \geq 20$ mm) do not contribute to emf induction. Similar to coil-RR, coil-RL (Figure 2b) also exhibits two peaks of $d\varphi/dz$ when the magnet moves to the edges of the coil, and the two peaks are on the same direction. However, while the magnet travels through the center of coil-RL, a peak appears in the opposite direction and is twice as high as the coil-end peaks. All three peaks rise in intensity rapidly as W increases from 10 mm to 30 mm, but they transition into a plateau as W further widens to 50 mm.

With profiles of $d\varphi/dz$ and a defined magnetic motion, the output voltage of EMGs at different coil widths can be calculated based on Equation (1). Experiments were carried out to verify the simulation and identify the optimum W for the EMGs. Specifically, single-layer coil of certain width in either RR or RL winding direction was placed on the middle of a linear frame (140 mm in height) (Figure S3a). A magnet went through a free drop inside the linear EMG, during which the generated open-circuit voltage was recorded with a Keithley 6514 electrometer (Tektronix, Inc., Beaverton, OR, USA). The simulation algorithm has been implemented in MATLAB with the differential equation of motion solved by ODE45 [35]. Here, EMGs with W ranging from 10 mm to 50 mm were studied. As shown in Figures 2, S1 and S2, the simulated output voltage for both coil-RR and coil-RL fits well with our experimental data, indicating the validity of the mathematical model used in simulation. The experimentally measured and calculated root mean square voltage (V_{rms}) and the average power (P_{avg}, $P_{avg} = \frac{{V_{rms}}^2}{R_{coil}}$) of these EMGs at different coil widths and winding directions are calculated and compared in Figure 2d.

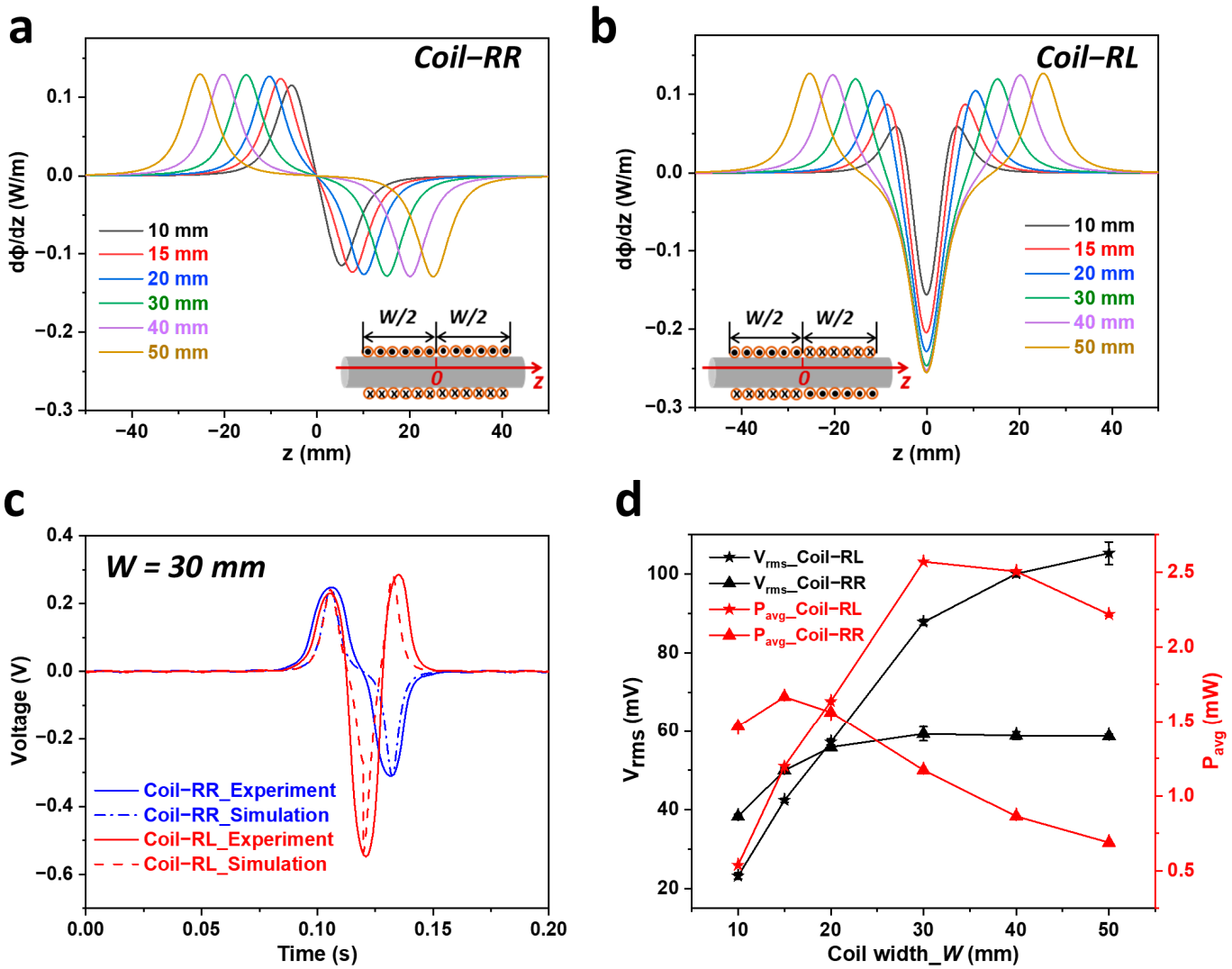

Figure 2. (**a**) Simulated magnetic flux gradient ($d\varphi/dz$) with respect to the relative displacement (z) of a magnet within coil-RR in different widths; (**b**) simulated magnetic flux gradient ($d\varphi/dz$) with respect to the relative displacement (z) of a magnet within coil-RL in different widths; (**c**) experimental and simulated open-circuit voltage of EMGs wound with 30 mm wide coil-RR and coil-RL, respectively; (**d**) experimentally measured and calculated V_{rms} and P_{avg} of EMGs in different widths of coil-RR and coil-RL, respectively.

For EMGs with coil-RR, V_{rms} increases slowly as W increases from 10 mm to 30 mm and, then, it reaches a plateau around 60 mV when W extends over 30 mm to 50 mm. The additional turns in extended coil width from 30 mm to 50 mm, corresponding to the ineffective middle region with kt close to 0 (Figure 2a), do not contribute to energy transduction but still add to the coil resistance. As a result, in terms of power output, EMG with W of 15 mm offers the highest P_{avg} of 1.75 mW due to its balanced V_{rms} and Rcoil. In comparison, the V_{rms} of coil-RL is only half of that of coil-RR when W is 10 mm but increases rapidly as W increases, surpassing coil-RR at W = 20 mm. It reaches 88 mV when W is 30 mm, then growing at a lower rate to 107 mV as W reaches 50 mm, which is twice as high as that of coil-RR at the same W. In terms of P_{avg} after considering Rcoil, coil-RL with W of 30 mm present the highest power output of 2.6 mW.

A coil with W of 30 mm can be considered as two 15 mm wide coil segments sitting adjacent to each other with the gap distance (d) of 0 mm (Figure S3b). The voltage output profile for coil in 30 mm is the overlay of voltage output from both 15 mm wide coil segments. By varying d, we can clearly see the effect of coil winding pattern on the

evolution of *kt* and resulting output voltage. As demonstrated in the simulation of *kt* from different *d* in Figure S4a,b, the *kt* of two neighboring coils add up under RL winding combination (two coil segments in opposite directions), whereas they cancel out each other under RR winding (two coil segments in the same direction). Both the adding-up and cancelling-out effects are enhanced as the coil segments sit closer to each other (decreasing *d*), therefore, resulting in the highest and lowest V_{rms} for coil-RL and coil-RR, respectively, when *d* is 0 mm (Figure S4c). We can also see that, as *d* increases to 30 mm, RR and RL winding provide almost the same values of V_{rms} (Figure S4c), since 30 mm is large enough to diminish the interference between the two neighboring segments. In summary, 30 mm coils composed of two oppositely wound segments (coil-RL) will bring the optimum *kt* for energy transduction.

2.2. Design of EMG Frame

The shape of EMG frame dictates the moving trajectory of the magnet, thus deciding its velocity upon various arm motions. Here, three different shapes of EMG frames are investigated and compared, including the conventional linear EMG (EMG-L), helix EMG (EMG-H), and the linear–helix combined EMG (EMG-LH) (Figure S5a–c). The heights of all EMGs are set to be 140 mm, about half of the mean length of human forearms [36], and the helix diameter is set to be 65 mm to fit the average human wrist [37]. As for EMG-LH, the heights of linear and helix parts are 100 mm and 15 mm, respectively, with a curved transition in between, which is 25 mm in height. Different frame configurations can be readily fabricated via 3D printing in our lab (detailed geometric parameters in Table S1). Several coil-RLs with *W* = 30 mm are wound outside of the EMG frames, with a 30 mm gap in between neighboring coils to avoid any interference. The stacked magnets can conform to the helix curvature (Figure S5d), resulting in an arc height of 9 mm which is smaller than the frame inner diameter (10 mm), thus ensuring they travel smoothly in both the helix and straight parts.

To compare the voltage output profiles as magnet travels through EMGs in different geometries, the free-drop motion of a magnet is investigated in each type of EMG, which imitates the magnet movement from arm lifting to some extent. In these experiments, the magnet is slid/dropped down from the top of EMG frames and moves inside each frame upon gravity when all coils are serially connected. Figure 3 compares the experimental and simulated results of the open-circuit voltage output in three EMG configurations. In EMG-L, the magnet only takes ca. 0.2 s to drop across its entire length, 140 mm, which holds only two coil segments. EMG-H with the highest length can amount to seven coils and it takes the magnet ca. 0.8 s to go through. The EMG-H extends the energy harvesting duration for each motion cycle, which is closer to human motion frequency. However, the lower velocity of the magnet in EMG-H results in 2.3 times lower peak voltage than that from EMG-L and, thus, compromises the instantaneous power output. EMG-LH combines the benefits of both EMG-L and EMG-H, keeping the linear part the same as that of EMG-L and continuing with a revolution of helix that can accommodate an additional three coils to continue harvesting kinetic energy from the moving magnet. It takes about 0.5 s for the magnet to reach the bottom of EMG-LH (mount with five coil segments), during which it can generate the same peak voltage and additional voltage waveforms as compared to EMG-L. By analyzing both the electromagnetic and mechanical systems of each EMG, we have simulated the instantaneous voltage output as magnet moving across coils in these different EMG configurations. According to Newton's second law of motion, the equations of motion for magnet movement in different EMG geometries can be established (details in supporting information). The simulated waveforms of output voltage (Figure 3, red curves) can fit with the experimental results to a large extent, with small deviations in the peak regions. These discrepancies may be caused by factors that are not yet accurately represented in the current simulation model, such as the magnetic moment variation of the magnets used. The simulation capability can be used to guide the customized device design, enabling the adaptation of EMG parameters to individual forearm features.

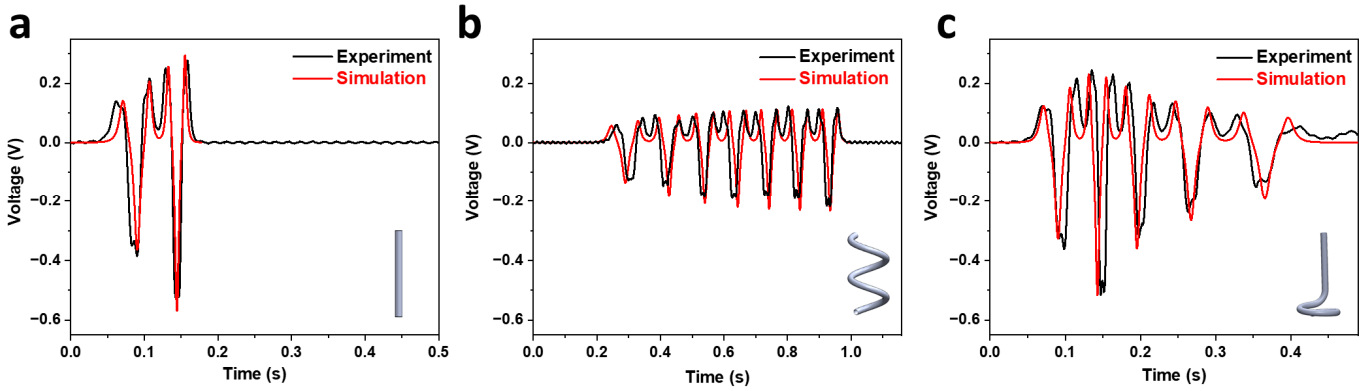

Figure 3. Experimental and simulated open-circuit voltage output of different EMGs: (**a**) EMG-L; (**b**) EMG-H; (**c**) EMG-LH.

2.3. Performance of EMGs upon Various Arm Motions

To minimize the energy loss upon magnet collision with the ends of the frames, compressible end stoppers are introduced. The compressible structure (Figure 1e) is constructed via 3D printing of TPU with 10% infill density of a gyroid pattern. To demonstrate the effectiveness of the stopper, a magnet is dropped from the top of an EMG-L. Compared to the EMG-L without compressible stopper, as shown in Figure S6, partial recovery of the kinetic energy of the magnet is observed, which is then transferred into electrical energy. To convert AC that is directly generated from EMGs into DC for practical applications, a full wave rectifier circuit (Figure S7) is connected to the EMGs. For the magnet motion of one free drop, the voltage and current at a load of 220 Ω are compared as shown in Figure S8a,b. Obviously, EMG-LH generates the highest P_{avg} ($P_{avg} = V_{rms} \times I_{rms}$) of 0.571 mW, followed by EMG-L of 0.522 mW and EMG-H of 0.139 mW, respectively.

Apart from free-drop motion that mimics arm lifting, EMG-LH also shows its advantages in other arm motions, such as arm lateral movement and arm swing. When arms move laterally (along *x* axis, Figure 1a) with the axis of EMGs parallel to the ground level (plane XY), the magnet is constrained in EMG-L but can move freely within the helix-shaped frames in both EMG-H and EMG-LH. Compared to EMG-H, EMG-LH with lower helix angle offers the magnet higher tangential velocity. As a result, EMG-LH generates the highest power of 0.273 mW, followed by EMG-H (0.10 mW) and EMG-L (ca. 0 mW) under lateral arm motion (Figure 4a,b). When arms swing (along Y axis, Figure 1b) during walking with straight elbows, the axis of the EMGs is perpendicular to the ground level (plane XY). There is no voltage or current generated in EMG-L and EMG-H (Figure 4c,d), since the magnets are stuck at the bottom of both frames. In contrast, the small slope of helix in EMG-LH allows the magnets to move across coils along the helix tube, resulting in steady voltage and current output (Figure 4c,d). Under external vibration frequency of 2 Hz and amplitude of 6 cm (controlled by a linear motor LinMot C1100 in our lab, as shown in Figure S9), EMG-LH can generate power (P_{avg}) of 0.179 mW (V_{rms} and I_{rms} of 127.5 mV and 1.407 mA, respectively). When arms swing (along *y* axis, Figure 1c) with bent elbow, the magnet can only oscillate in the linear frame. Therefore, as shown in Figure 4e,f, EMG-L and EMG-LH can generate comparable power of 1.338 mW under the external vibration frequency of 2 Hz and amplitude of 6 cm. Besides linear motion along certain axes, EMGs with curved helix shapes can also harvest energy by rotating frames. Under regular wrist rotation (Figure 1e), EMG-H and EMG-LH can generate comparable power of 1.232 mW and 1.187 mW, respectively (Figure S8c,d).

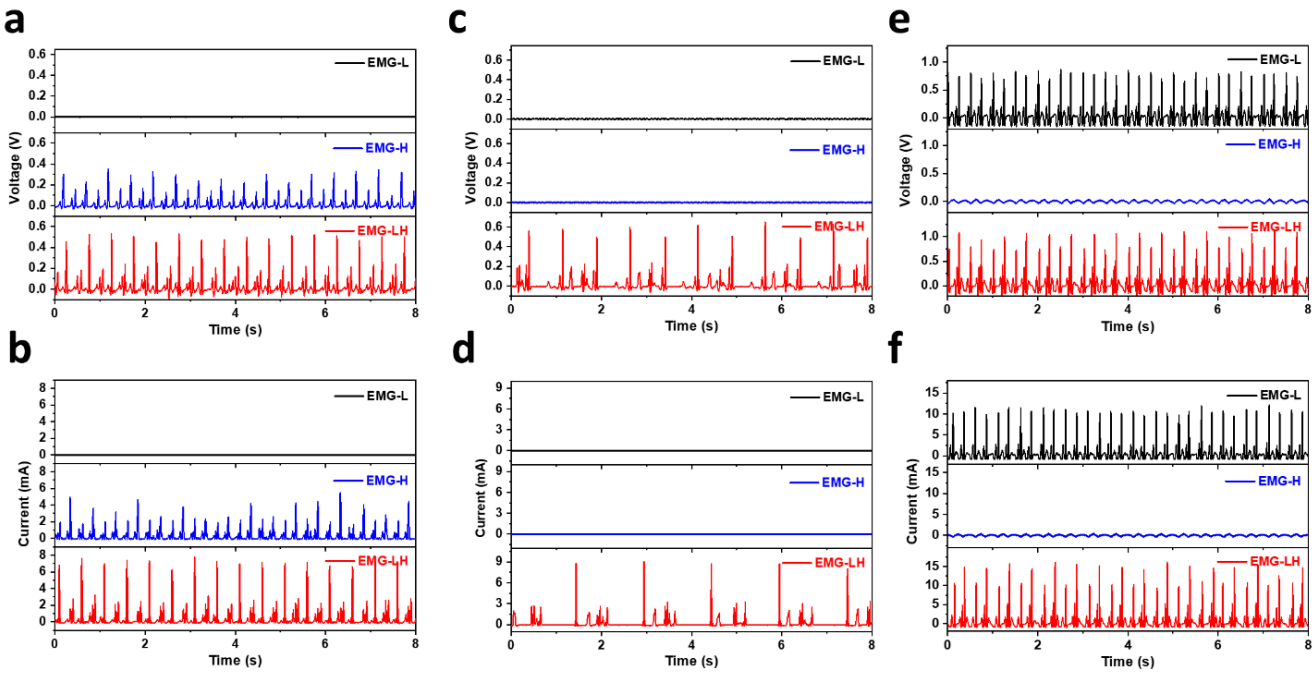

Figure 4. Output performance of EMG-L, EMG-H, and EMG-LH connected circuits when the EMG frames move in different directions under exciting vibration frequency of 2 Hz and amplitude of 6 cm. (**a**,**b**) Voltage (**a**) and current (**b**) of load R when EMG frames oscillate along axis *x* with frame axes parallel to plane XY (as in Figure 1a); (**c**,**d**) voltage (**c**) and current (**d**) of load R when EMG frames oscillate along axis *y* with frame axes perpendicular to plane XY (as in Figure 1b); (**e**,**f**) voltage (**e**) and current (**f**) of load R when EMG frames oscillate along axis Y with frame axes parallel to plane XY (as in Figure 1c).

In comparison with helix-shaped EMG, EMG-L can offer higher tangential velocity of magnet and, thus, higher peak voltage. However, the magnet housed in linear frames exhibits a very limited degree of freedom, resulting in poor energy-harvest efficiency in other forearm motions. EMG-H can offer higher degree of motion freedoms for magnets upon arm movements; however, it lowers the tangential velocity of the magnet, thus compromising the instantaneous power output. EMG-LH with frames in combination of linear and helix geometries can well adapt to various arm motions and maintain high velocity of magnet along different directions, therefore, effectively harvesting biomechanical energy from daily upper-body motions.

To further demonstrate the practical application of the EMG-LH, we have investigated its ability to charge capacitors and batteries. The charging behavior of a capacitor (470 μF, 25 V) by the EMG-LH under regular forearm movements in different motions are shown in Figure 5a,b. Specifically, within 5 s, the capacitor can be charged to 2.8 V under forearm rotation, 2.0 V under forearm movement along *y* axis with bent elbow, 1.65 V under forearm movement along *x* axis, 1.2 V under arm movement along *y* axis with straight elbow, and 0.75 V under arm movement along Z axis, respectively. Practically, many electronics require a regulated charging voltage at certain level. Here, a power management circuit (Figure S10) with a step-up DC/DC converter (LT1302) is adopted to deliver a constant DC voltage of 5 V, which is compatible with lithium-ion polymer (LiPo) batteries [7]. Figure 5c shows the 5 V voltage output of EMG-LH under forearm rotation and forearm movement along the *y* axis with bent elbow, respectively, indicating its ability to charge LiPo batteries. As demonstrated in Figure 5d, a LiPo battery of 0.1 Wh can be charged from 3.0 V to 3.2 V within 10 min under continuous forearm movement along the *y* axis with bent elbow with our EMG-LH which weighs 42.79 g.

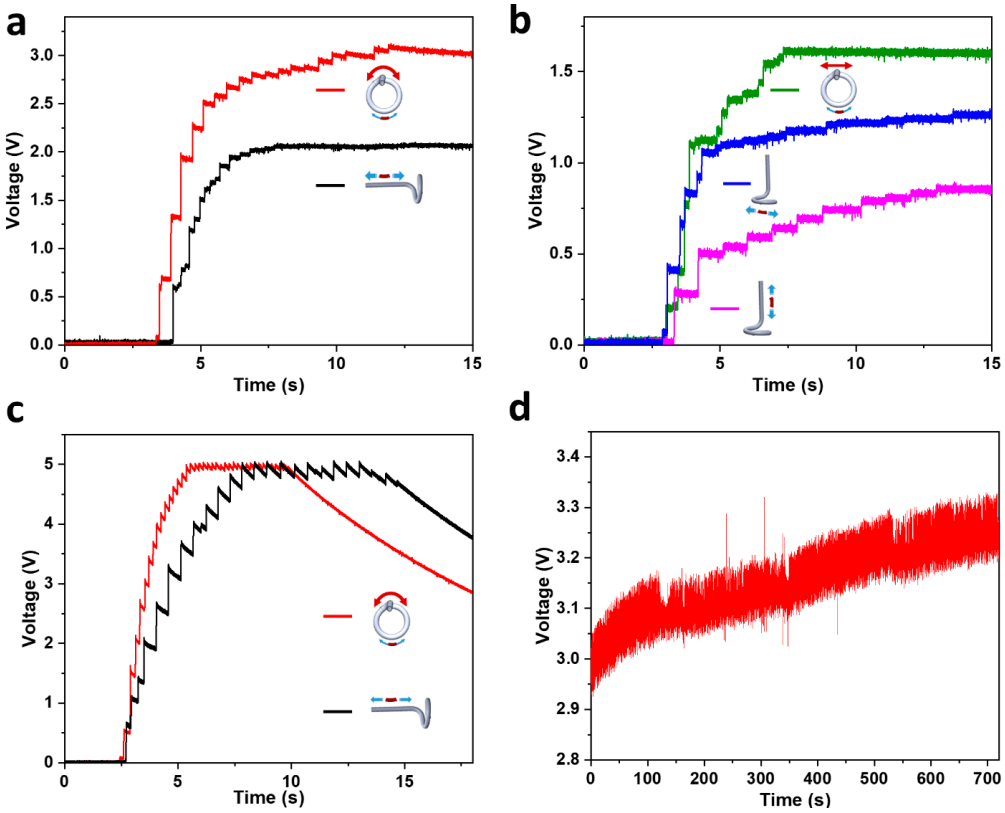

Figure 5. (**a**) Measured voltage profile of a capacitor (470 μF) being charged by an EMG-LH under forearm rotation and forearm movement along *y* axis with a bent elbow, respectively; (**b**) measured voltage evolution of a capacitor (470 μF) being charged by an EMG-LH under forearm movement along *x* axis, along *y* axis with a straight elbow, and along *z* axis, respectively; (**c**) output voltage of the EMG-LH rectified by a power management circuit under forearm rotation and forearm movement along *y* axis with a bent elbow, respectively; (**d**) measured voltage profile of a LiPo battery (0.1 Wh) being charged by the EMG-LH, as rectified by the same power management circuit, under forearm movement along *y* axis with bent elbow.

3. Conclusions

Here, we have presented a wearable EMG design in a unique "linear and helix combined" geometry, which can function as a multidirectional energy harvester from daily forearm motions in a more effective manner. Numerical simulation is adopted to correlate magnet/coil configurations and EMG output, which is later used to guide the design of coil winding patterns to maximize the EMG output. In addition, a good match between the simulated results and experimental data has been achieved in all three EMG configurations, further consolidating our design strategy. Compared to EMG-L and EMG-H that can only harvest energy in limited arm motions, the combination of linear and helix-shaped frames enables EMG-LHs to adapt to all kinds of forearm motions, rendering magnet and coil relative vibrations for power generation. We have also demonstrated the successful charging of capacitors and LiPo batteries by EMG-LHs for practical applications. This work indicates the feasibility of customized design of wearable EMGs on an individual basis, as guided by numerical simulations in a forearm-motion setting.

Supplementary Materials: The following supporting information can be downloaded at: https://www.mdpi.com/article/10.3390/act12060225/s1, Table S1: Parameters of magnet, coil, and frames; Figure S1: Experimental and simulated open-circuit voltage output of EMGs with various widths of coil-RR. (a) 1 cm; (b) 1.5 cm; (c) 2 cm; (d) 3 cm; (e) 4 cm; (f) 5 cm; Figure S2: Experimental and simulated open-circuit voltage output of EMGs with various widths of coil-RL. (a) 1 cm; (b) 1.5 cm; (c) 2 cm; (d) 3 cm; (e) 4 cm; (f) 5 cm; Figure S3: Schematics of straight-shaped EMGs with (a) one

coil wound in the middle and (b) one coil divided into two half-wide coil segments separated with certain distance (d); Figure S4: (a,b) The relationship between $d\varphi/dz$ and z under various distances (d) (0–30 mm) between two 1.5 cm wide coil segments in opposite winding direction (a) and same winding direction (b), respectively; (c) V_{rms} and P_{avg} of EMGs under various distances between two 1.5 cm wide coil segments and different winding direction combinations; (d–k) open-circuit voltage output of EMGs with two coil segments under various distances between two segments and different winding direction combinations: (d) same direction with d of 0 mm; (e) same direction with d of 10 mm; (f) same direction with d of 20 mm; (g) same direction with d of 30 mm; (h) opposite direction with d of 0 mm; (i) opposite direction with d of 10 mm; (j) opposite direction with d of 20 mm; (k) opposite direction with d of 30 mm; Figure S5: Photographs of as-fabricated (a) linear EMG (EMG-L) equipped with compressible end-stopper; (b) helix EMG (EMG-H) wore on forearm; (c) linear–helix combined EMG (EMG-LH) wore on forearm; (d) photographs of stacked magnets in straight (top) and curved (bottom) alignments, respectively; Figure S6: Open-circuit voltage of EMG-Ls with and without compressible end stoppers in one free drop of magnet; Figure S7: Full-wave rectifier circuit with each AC generated from one coil connected to two diodes; Figure S8: (a) Voltage and (b) current of load R from EMG-L, EMG-H, and EMG-LH connected circuits in one free drop of magnets; (c) voltage; and (d) current of load R from EMG-L, EMG-H, and EMG-LH connected circuits under forearm rotation; Figure S9. Photograph of the equipment setup including Linear motor LinMot for controlling linear movement and Keithley Meter for voltage and current measurement; Figure S10: (a) Schematic diagram of the power management circuit for DC/DC voltage stepping up; (b) photograph of the assembled printed circuit board (PCB) of the power management circuit.

Author Contributions: Data curation, N.H.; Funding acquisition, F.Z.; Investigation, N.H., C.K. and Q.X.; Supervision, W.G. and F.Z.; Project Administration, F.Z.; Writing—original draft, N.H.; Writing—review and editing, W.G. All authors have read and agreed to the published version of the manuscript.

Funding: This research was funded by United States Army (Grant Nos. W911NF19C0074 and W911NF18C0086).

Data Availability Statement: Not applicable.

Conflicts of Interest: The authors declare no conflict of interest.

References

1. Xu, C.; Song, Y.; Han, M.; Zhang, H. Portable and Wearable Self-Powered Systems Based on Emerging Energy Harvesting Technology. *Microsyst. Nanoeng.* **2021**, *7*, 25. [CrossRef]
2. Zeng, X.; Peng, R.; Fan, Z.; Lin, Y. Self-Powered and Wearable Biosensors for Healthcare. *Mater. Today Energy* **2022**, *23*, 100900. [CrossRef]
3. Gao, M.; Wang, P.; Jiang, L.; Wang, B.; Yao, Y.; Liu, S.; Chu, D.; Cheng, W.; Lu, Y. Power Generation for Wearable Systems. *Energy Environ. Sci.* **2021**, *14*, 2114–2157. [CrossRef]
4. Choi, Y.-M.; Lee, M.G.; Jeon, Y. Wearable Biomechanical Energy Harvesting Technologies. *Energies* **2017**, *10*, 1483. [CrossRef]
5. Liu, M.; Qian, F.; Mi, J.; Zuo, L. Biomechanical Energy Harvesting for Wearable and Mobile Devices: State-of-the-Art and Future Directions. *Appl. Energy* **2022**, *321*, 119379. [CrossRef]
6. Zhang, Y.; Luo, A.; Wang, Y.; Dai, X.; Lu, Y.; Wang, F. Rotational Electromagnetic Energy Harvester for Human Motion Application at Low Frequency. *Appl. Phys. Lett.* **2020**, *116*, 053902. [CrossRef]
7. Toyabur Rahman, M.; Sohel Rana, S.; Salauddin, M.; Maharjan, P.; Bhatta, T.; Kim, H.; Cho, H.; Park, J.Y. A Highly Miniaturized Freestanding Kinetic-Impact-Based Non-Resonant Hybridized Electromagnetic-Triboelectric Nanogenerator for Human Induced Vibrations Harvesting. *Appl. Energy* **2020**, *279*, 115799. [CrossRef]
8. Liu, Y.; Khanbareh, H.; Halim, M.A.; Feeney, A.; Zhang, X.; Heidari, H.; Ghannam, R. Piezoelectric Energy Harvesting for Self-Powered Wearable Upper Limb Applications. *Nano Sel.* **2021**, *2*, 1459–1479. [CrossRef]
9. Zhou, D.; Wang, N.; Yang, T.; Wang, L.; Cao, X.; Wang, Z.L. A Piezoelectric Nanogenerator Promotes Highly Stretchable and Self-Chargeable Supercapacitors. *Mater. Horiz.* **2020**, *7*, 2158–2167. [CrossRef]
10. Fan, F.-R.; Tian, Z.-Q.; Lin Wang, Z. Flexible Triboelectric Generator. *Nano Energy* **2012**, *1*, 328–334. [CrossRef]
11. Walden, R.; Aazem, I.; Babu, A.; Pillai, S.C. Textile-Triboelectric Nanogenerators (T-TENGs) for Wearable Energy Harvesting Devices. *Chem. Eng. J.* **2023**, *451*, 138741. [CrossRef]
12. Khan, A.S.; Khan, F.U. A Survey of Wearable Energy Harvesting Systems. *Int. J. Energy Res.* **2022**, *46*, 2277–2329. [CrossRef]
13. Luo, J.; Gao, W.; Wang, Z.L. The Triboelectric Nanogenerator as an Innovative Technology toward Intelligent Sports. *Adv. Mater.* **2021**, *33*, 2004178. [CrossRef]

14. Iqbal, M.; Nauman, M.M.; Khan, F.U.; Abas, P.E.; Cheok, Q.; Iqbal, A.; Aissa, B. Vibration-Based Piezoelectric, Electromagnetic, and Hybrid Energy Harvesters for Microsystems Applications: A Contributed Review. *Int. J. Energy Res.* **2021**, *45*, 65–102. [CrossRef]
15. Williams, C.B.; Yates, R.B. Analysis of a Micro-Electric Generator for Microsystems. *Sens. Actuators A Phys.* **1996**, *52*, 8–11. [CrossRef]
16. Spreemann, D.; Hoffmann, D.; Folkmer, B.; Manoli, Y. Numerical Optimization Approach for Resonant Electromagnetic Vibration Transducer Designed for Random Vibration. *J. Micromech. Microeng.* **2008**, *18*, 104001. [CrossRef]
17. Saha, C.R.; O'Donnell, T.; Wang, N.; McCloskey, P. Electromagnetic Generator for Harvesting Energy from Human Motion. *Sens. Actuators A Phys.* **2008**, *147*, 248–253. [CrossRef]
18. Nguyen, D.S.; Halvorsen, E.; Jensen, G.U.; Vogl, A. Fabrication and Characterization of a Wideband MEMS Energy Harvester Utilizing Nonlinear Springs. *J. Micromech. Microeng.* **2010**, *20*, 125009. [CrossRef]
19. Harne, R.L.; Wang, K.W. A Review of the Recent Research on Vibration Energy Harvesting via Bistable Systems. *Smart Mater. Struct.* **2013**, *22*, 023001. [CrossRef]
20. Foisal, A.R.M.; Hong, C.; Chung, G.-S. Multi-Frequency Electromagnetic Energy Harvester Using a Magnetic Spring Cantilever. *Sens. Actuators A Phys.* **2012**, *182*, 106–113. [CrossRef]
21. Halim, M.A.; Cho, H.; Park, J.Y. Design and Experiment of a Human-Limb Driven, Frequency up-Converted Electromagnetic Energy Harvester. *Energy Convers. Manag.* **2015**, *106*, 393–404. [CrossRef]
22. Kulah, H.; Najafi, K. Energy Scavenging From Low-Frequency Vibrations by Using Frequency Up-Conversion for Wireless Sensor Applications. *IEEE Sens. J.* **2008**, *8*, 261–268. [CrossRef]
23. Haroun, A.; Yamada, I.; Warisawa, S. Study of Electromagnetic Vibration Energy Harvesting with Free/Impact Motion for Low Frequency Operation. *J. Sound Vib.* **2015**, *349*, 389–402. [CrossRef]
24. Zelik, K.E.; Takahashi, K.Z.; Sawicki, G.S. Six Degree-of-Freedom Analysis of Hip, Knee, Ankle and Foot Provides Updated Understanding of Biomechanical Work during Human Walking. *J. Exp. Biol.* **2015**, *218*, 876–886. [CrossRef]
25. Samad, F.A.; Karim, M.F.; Paulose, V.; Ong, L.C. A Curved Electromagnetic Energy Harvesting System for Wearable Electronics. *IEEE Sens. J.* **2016**, *16*, 1969–1974. [CrossRef]
26. Maharjan, P.; Bhatta, T.; Salauddin Rasel, M.; Salauddin, M.; Toyabur Rahman, M.; Park, J.Y. High-Performance Cycloid Inspired Wearable Electromagnetic Energy Harvester for Scavenging Human Motion Energy. *Appl. Energy* **2019**, *256*, 113987. [CrossRef]
27. Wu, Z.; Tang, J.; Zhang, X.; Yu, Z. An Energy Harvesting Bracelet. *Appl. Phys. Lett.* **2017**, *111*, 013903. [CrossRef]
28. Maharjan, P.; Toyabur, R.M.; Park, J.Y. A Human Locomotion Inspired Hybrid Nanogenerator for Wrist-Wearable Electronic Device and Sensor Applications. *Nano Energy* **2018**, *46*, 383–395. [CrossRef]
29. Li, Z.; Yan, Z.; Luo, J.; Yang, Z. Performance Comparison of Electromagnetic Energy Harvesters Based on Magnet Arrays of Alternating Polarity and Configuration. *Energy Convers. Manag.* **2019**, *179*, 132–140. [CrossRef]
30. Li, Z.; Luo, J.; Xie, S.; Xin, L.; Guo, H.; Pu, H.; Yin, P.; Xu, Z.; Zhang, D.; Peng, Y.; et al. Instantaneous Peak 2.1 W-Level Hybrid Energy Harvesting from Human Motions for Self-Charging Battery-Powered Electronics. *Nano Energy* **2021**, *81*, 105629. [CrossRef]
31. Wang, W.; Wei, H.; Wei, Z.-H. Numerical Analysis of a Magnetic-Spring-Based Piecewise Nonlinear Electromagnetic Energy Harvester. *Eur. Phys. J. Plus* **2021**, *137*, 56. [CrossRef]
32. Haroun, A.; Yamada, I.; Warisawa, S. Micro Electromagnetic Vibration Energy Harvester Based on Free/Impact Motion for Low Frequency–Large Amplitude Operation. *Sens. Actuators A Phys.* **2015**, *224*, 87–98. [CrossRef]
33. Beeby, S.P.; O'Donnell, T. Electromagnetic Energy Harvesting. In *Energy Harvesting Technologies*; Priya, S., Inman, D.J., Eds.; Springer: Boston, MA, USA, 2009; pp. 129–161. ISBN 978-0-387-76464-1.
34. Chow, T.L. *Introduction to Electromagnetic Theory: A Modern Perspective*; Jones & Bartlett Learning: Burlington, MA, USA, 2006; ISBN 0-7637-3827-1.
35. Solve Nonstiff Differential Equations—Medium Order Method—MATLAB Ode45. Available online: https://www.mathworks.com/help/matlab/ref/ode45.html (accessed on 9 November 2022).
36. Zarzycka, N.; Załuska, S. Measurements of the forearm i inhabitants of the Lublin region. In *Annales Universitatis Mariae Curie-Sklodowska. Sectio D: Medicina*; Uniwersytetu Marii Curie Sklodowskies: Lublin, Poland, 1989; Volume 44, pp. 85–92.
37. Kim, H.; Jeong, S. Case Study: Hybrid Model for the Customized Wrist Orthosis Using 3D Printing. *J. Mech. Sci. Technol.* **2015**, *29*, 5151–5156. [CrossRef]